Journal of Materials Chemistry C

ROYAL SOCIETY OF CHEMISTRY

PAPER

Published on 27 July 2026
Licence and permissions

Cite this: DOI: 10.1039/d6tc02069k

Beyond dipole strength: interfacial charge-transfer kinetics govern device efficiency at SAM/ITO interfaces

Hitakshi Singh and Anirban Mondal *

Received 23rd June 2026,
Accepted 24th July 2026

DOI: 10.1039/d6tc02069k

rsc.li/materials-c

Efficient charge extraction at electrode/organic interfaces is a critical determinant of performance in organic optoelectronic devices, yet the molecular-level descriptors governing this process remain inadequately defined. In this work, we present a comprehensive structure–property–kinetics framework to elucidate how chemical functionalization of self-assembled monolayers (SAMs) modulates interfacial charge transport at SAM-modified ITO electrodes. By systematically integrating dipole moment analysis, electrostatic potential (ESP) mapping, energy-level alignment, and electronic coupling calculations, we demonstrate that commonly invoked descriptors such as dipole magnitude or work function shifts alone do not reliably predict interfacial performance. Instead, charge-transfer kinetics, evaluated within the Marcus–Hush formalism using POD-derived coupling elements, emerge as a physically meaningful and predictive metric that intrinsically captures the synergy between energetic driving force and interfacial hybridization. Strong electron-withdrawing substituents enhance molecular polarization and tune HOMO alignment relative to the ITO Fermi level, but their decisive impact arises from simultaneously strengthening molecule–substrate coupling. Among the investigated systems, JJ27–NO_2 exhibits the largest dipole moment, pronounced ESP asymmetry, strong interfacial coupling, and the highest computed hole-transfer rate constant, identifying it as the most efficient charge-extraction layer. Importantly, the calculated rate constants qualitatively correlate with experimentally reported power conversion efficiencies, establishing a direct structure–kinetics–performance relationship. By moving beyond isolated electrostatic descriptors and introducing interfacial charge-transfer rate as a unified performance metric, this study provides a predictive design principle for engineering next-generation SAM/electrode interfaces for high-efficiency organic optoelectronics.

1 Introduction

Organic electronics has attracted sustained interest due to its potential for low-cost, lightweight, flexible, and mechanically conformable optoelectronic devices.[1–3] Organic semiconductors (OSCs) form active layers in organic photovoltaic (OPV) devices, where their performance is governed not only by bulk material properties but predominantly by the electronic structure of interfaces. Unlike inorganic semiconductors, photoexcitation in OSCs produces tightly bound electron–hole pairs, or excitons, as a consequence of their low dielectric constants ($\epsilon \approx 3-4$). These excitons exhibit substantial Coulombic binding energies (0.3–0.5 eV), necessitating efficient interfacial processes to achieve charge separation.[4,5] In conventional OPV architectures, exciton dissociation occurs predominantly at donor–acceptor heterojunctions, driven by the energetic offset between the donor highest occupied molecular orbital (HOMO) and the acceptor lowest unoccupied molecular orbital (LUMO). However, it is now well established that energy-level offsets alone are insufficient to completely describe interfacial charge-transfer processes.[6,7] Charge generation, separation, and extraction are strongly influenced by interfacial morphology, electronic coupling, and dynamic charge redistribution.[8]

While energy-level alignment at donor–acceptor interfaces governs exciton dissociation, appropriate alignment at the organic semiconductor/inorganic electrode interface is equally critical for efficient charge extraction.[9–12] Davis *et al.* emphasized that both charge generation and charge extraction efficiencies are dictated by energy-level alignment at internal heterojunctions and external electrode contacts, respectively.[13] In particular, poor electronic coupling or unfavorable energetic alignment at electrode/organic interfaces introduces contact resistance, thereby degrading the fill factor and overall device efficiency.[14,15] To mitigate these losses, interlayers, such as conducting polymers, metal oxides, or dipolar small molecules are frequently

Department of Chemistry, Indian Institute of Technology Gandhinagar, Gujarat, 382355, India. E-mail: amondal@iitgn.ac.in

employed to improve selectivity and suppress interfacial recombination.[16]

Among the various strategies for contact engineering, the use of dipolar modifiers and self-assembled monolayers (SAMs) has emerged as a powerful molecular-level approach for tuning electrode work functions.[17] SAMs form ordered, single-molecule-thick films on electrode surfaces, and their intrinsic dipole moments induce vacuum-level shifts that modulate the effective work function of the electrode.[18] For example, substituted benzyl phosphonic acids have been shown to tune the indium–tin–oxide (ITO) work function over a range approaching 2 eV, enabling near-ohmic contacts for both hole- and electron-selective interfaces.[19] While conductive polymers such as PEDOT:PSS remain widely used as hole-transport layers, however, their high acidity and hygroscopic nature raise concerns regarding long-term device stability.[20–22] These considerations underscore the need for chemically robust, electronically selective interlayers that can simultaneously reduce contact resistance and enhance device reliability.

In this context, Jiang *et al.* demonstrated that selectively halogenated carbazole-based SAMs can significantly enhance OPV performance by simultaneously increasing molecular dipole strength, film stability, and packing density.[19] By introducing bromine substituents at chemically inert positions on a helical 7H-dibenzo[*c*,*g*]carbazole framework, the authors developed a series of SAM molecules with systematically varied dipole moments. Devices incorporating the JJ26 SAM as the hole extraction layer achieved power conversion efficiencies (PCEs) exceeding 19%. The underlying interpretation linked enhanced PCE to increased molecular dipole strength, which was proposed to lower the effective ITO work function when dipoles are oriented toward the substrate, thereby facilitating hole extraction.

Despite these promising experimental observations, a closer inspection of the reported dataset reveals that power conversion efficiency does not follow a monotonic or universal trend with the isolated-molecule dipole moment. This inconsistency indicates that dipole magnitude alone is insufficient to serve as a predictive descriptor of interfacial charge-transfer efficiency. While dipole-induced work-function modulation is an important macroscopic effect, interfacial charge extraction is fundamentally governed by microscopic quantities: namely, the energetic alignment of interfacial states and the strength of electronic coupling across the contact. Previous theoretical investigations have demonstrated that charge-transfer rates at organic interfaces depend jointly on the interfacial energy offset (ΔE) and the electronic coupling matrix element [$J(E)$], and that neither quantity independently captures contact resistance.[23,24] Within a Marcus-type framework, these parameters collectively determine the charge-transfer rate constant, providing a rigorous route to connect interfacial electronic structure with experimentally measurable transport characteristics. Such a perspective shifts the focus from isolated molecular properties to the electronic structure of the assembled interface.

In this work, we adopt this microscopic viewpoint to interrogate charge extraction at the ITO/organic semiconductor interface modified by carbazole-based self-assembled monolayers. Using density functional theory (DFT) combined with the Marcus–Hush formalism, we compute interfacial energy-level alignment, electronic coupling elements, and charge-transfer rate constants for the experimentally reported SAM molecules of Jiang *et al.*, alongside seven rationally designed analogues. By quantitatively correlating calculated charge-transfer rates with orbital alignment and coupling strength, we demonstrate that interfacial electronic structure, rather than dipole moment in isolation, governs charge-transfer efficiency. We further show that a composite descriptor derived from these microscopic parameters rationalizes the experimentally observed device trends. Importantly, the framework developed here is not limited to organic solar cells; it is transferable to other hybrid organic–inorganic interfaces, including SAM-modified contacts in perovskite solar cells, where interfacial energetics and coupling similarly dictate carrier extraction and recombination dynamics. The present study therefore establishes a broadly applicable, first-principles strategy for evaluating and designing molecular interlayers for next-generation photovoltaic and optoelectronic devices.

2 Methods

Electronic structure calculations were carried out within the framework of density functional theory.[25] As a first step, the geometries of the individual SAM molecules and the ITO electrode surface were optimized separately. Because charge transport in organic solar cells involves transient localization of charge on molecular units, the interlayer molecules were modeled as isolated monomeric ligands. In total, ten SAM molecules were considered in this study-three experimentally reported systems and seven rationally designed analogues introduced to systematically probe the role of molecular dipole moment (Fig. 1). The electrode was represented by a four-layer ITO slab. During structural optimization, the bottom two layers were kept fixed to mimic the bulk constraint of the electrode, while the upper two layers were allowed to relax fully. This approach ensures a realistic description of the electrode–SAM interface: the constrained layers preserve bulk-like structural integrity, whereas the relaxed surface layers remain free to reorganize and interact with the adsorbed ligand.

Because self-assembled monolayer molecules can adopt multiple adsorption geometries and orientations on the ITO surface, a single optimized structure may not adequately represent the thermally accessible interfacial configurations. Although the initial SAM–electrode geometry was optimized at the DFT, several low-energy conformations can exist in the vicinity of this minimum due to rotational, tilting, and lateral degrees of freedom of the ligand. To systematically sample this configurational space, the electrode atoms were held fixed to preserve the slab structure, and the equilibrium adsorption distance between the ligand anchoring group and the ITO surface was first identified from the optimized geometry. Around this equilibrium separation, a displacement window of ± 0.5 Å was introduced to account for

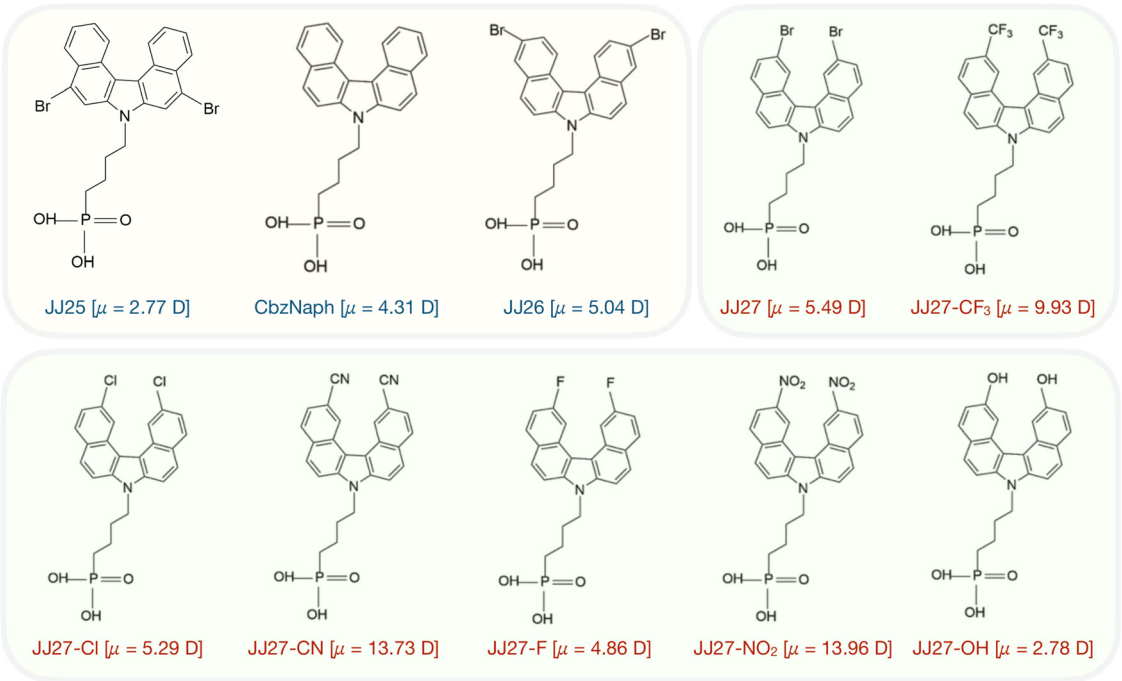

Fig. 1 Chemical structures and calculated dipole moments (μ, in Debye) of the phosphonic acid–functionalized carbazole-based SAM molecules investigated in this study. Experimentally reported reference systems: JJ25, CbzNaph, and JJ26. Rationally designed JJ27 derivatives featuring systematic substituent variations (Br, CF_3, Cl, CN, F, NO_2, and OH) introduced to modulate molecular dipole strength and interfacial electronic properties.

thermal fluctuations and slight variations in adsorption height. Within this window, 10 000 conformers were generated by randomly perturbing molecular orientations and interfacial geometrical parameters. The relative energies of these configurations were evaluated using the semi-empirical XTB-GFN-FF method,[26] enabling efficient screening of low-energy adsorption geometries prior to subsequent electronic-structure analysis. Among the sampled configurations, the geometry in which the ligand adopts a predominantly horizontal orientation relative to the ITO surface was found to be the most energetically favorable. This lowest-energy adsorption structure was therefore selected as the representative interfacial configuration and used for all subsequent electronic structure and charge-transfer calculations. To confirm that our overarching kinetic conclusions are robust and independent of this primary thermodynamic geometry, the computational model was further extended to evaluate an alternative, vertically aligned two-molecule configuration mimicking dense monolayer packing constraints. A comparative analysis of both spatial arrangements was performed to explicitly validate the invariance of our descriptor trends against alternative structural landscapes.

The electronic wave functions and nuclear coordinates were optimized to ensure numerical accuracy and reproducibility across all calculations. An electronic self-consistent field tolerance of 1.0×10^{-6} Ha and an iterative diagonalization tolerance of 1.0×10^{-8} were employed. Geometry optimizations were considered converged when the maximum force on any atom fell below 1.0×10^{-3} Ha $Bohr^{-1}$ and the maximum atomic displacement was less than 0.003 Å. All calculations were performed using the Quickstep module of the CP2K package.[27] Exchange–correlation effects were treated within the generalized gradient approximation using the Perdew–Burke–Ernzerhof (PBE) functional.[28] The auxiliary plane-wave expansion of the electron density employed a cutoff energy of 400 Ry. Valence electrons were described explicitly, while core electrons were represented using norm-conserving Goedecker–Teter–Hutter (GTH) pseudopotentials.[29,30] Kohn–Sham orbitals were expanded in a triple-ζ valence plus polarization (TZVP-MOLOPT-PBE-GTH) basis set for all atomic species. A Fermi–Dirac smearing scheme with an electronic temperature of 298.15 K was applied to ensure stable fractional occupation near the Fermi level in metal-surface calculations. Owing to the large supercell employed to model the slab interface, Brillouin zone sampling was restricted to the Γ point. These thresholds were consistently applied throughout all CP2K simulations. Unless otherwise specified, the density functional, basis sets, plane-wave cutoff, and pseudopotentials remained identical for geometry optimization, electronic structure analysis, and subsequent projector-operator diabatization (POD) calculations to maintain methodological consistency.

For the POD-based electronic coupling analysis, the entire organic ligand was defined as one fragment (donor block), and the full ITO slab was defined as the second fragment (acceptor block). The ET_Coupling module within CP2K was invoked through the Properties section to evaluate fragment-resolved energy levels and electronic coupling elements. In this scheme, molecular orbital cube files corresponding to the frontier orbitals (HOMO and LUMO) of each fragment were generated and projected onto the combined interface system. This procedure

yielded the relative energy alignment of the donor and acceptor states, as well as the orbital-specific electronic coupling matrix elements governing interfacial charge transfer.

The internal reorganization energy associated with hole transfer was computed using the four-point method,[31] which evaluates the energetic penalty arising from geometric relaxation between different charge states. For each SAM molecule, the neutral and cationic monomers were independently optimized to obtain their respective equilibrium geometries. Subsequently, single-point energy calculations were performed for each charge state at both optimized geometries, enabling the extraction of the intramolecular reorganization contribution from the corresponding energy differences. These calculations were carried out using the Gaussian 09 program[32] at the B3LYP level of theory with the def2-SVP basis set. Grimme's D3 empirical dispersion correction was included to account for long-range correlation effects.

Using the computed interfacial energy alignment, electronic coupling elements, and intramolecular reorganization energies, the electron-transfer rate between the SAM molecule and the electrode was evaluated within the Marcus–Hush formalism.[24] The rate constant is given by

$$k_{\mathrm{et}} = \frac{2\pi}{\hbar}\int J^2(E)\frac{1}{1+\exp\left(\dfrac{E-E_{\mathrm{F}}}{kT}\right)}n(E)\frac{1}{\sqrt{4\pi\lambda kT}} \times \exp\left[-\frac{(\lambda-\Delta E+q\eta)^2}{4\lambda kT}\right]\mathrm{d}E$$

where E_{F} denotes the Fermi level of the electrode, λ is the intramolecular reorganization energy of the ligand, and $n(E)$ represents the density of available electrode states at energy E. The term $J(E)$ corresponds to the energy-dependent electronic coupling between the relevant SAM orbital and the electrode states, while ΔE is defined as the energy difference between the ligand frontier level and the electrode state at energy E. The overpotential η accounts for any applied bias; in the absence of reliable experimental values for the present OSC–electrode systems, η was set to zero. The integral was evaluated over the unoccupied electrode states relevant for hole extraction. The reorganization energy λ was obtained for each ligand from the DFT-based four-point procedure described above. The electronic coupling function $J(E)$ was constructed by averaging the coupling between the SAM HOMO and all energetically degenerate electrode states at a given energy E. In this manner, the rate expression explicitly incorporates both the interfacial electronic structure and the nuclear reorganization penalty, enabling a quantitative assessment of charge-transfer kinetics at the SAM-modified electrode interface.

The work function of the SAM-modified ITO surface was evaluated using density functional theory as implemented in the Vienna Ab initio Simulation Package (VASP).[33] For this purpose, the optimized SAM molecules were adsorbed onto the ITO slab, and a vacuum region of 20 Å was introduced along the surface normal to eliminate spurious interactions between periodic images. A single-point SCF calculation was then performed with an electronic convergence threshold of 1×10^{-6} eV to accurately determine the electrostatic potential and Fermi level of the system. The vacuum level was extracted using the LVHAR tag, which outputs the Hartree and ionic contributions to the local electrostatic potential. A planar-averaged potential was computed along the direction perpendicular to the surface, and the asymptotic value in the vacuum region was identified as the vacuum potential. The work function Φ was subsequently determined from the difference between the vacuum potential and the Fermi level according to $\Phi = e \times V_{\mathrm{vacuum}} - E_{\mathrm{Fermi}}$, where e is the elementary charge, V_{vacuum} is the electrostatic potential in the vacuum region, and E_{F} is the Fermi energy of the slab system.

3 Results and discussion

To systematically probe the influence of substitution on the electronic structure and molecular polarization, we constructed a series of seven computationally designed derivatives based on the experimentally synthesized helical 7*H*-dibenzo[*c*,*g*]carbazole scaffold. The three reference systems; CbzNaph, JJ25 (5,9-dibromo), and JJ26 (3,11-dibromo), serve as experimentally validated benchmarks (Fig. 1). Building upon this core, additional derivatives were generated to enable controlled modulation of the molecular dipole moment through strategic peripheral functionalization.

Substituent-induced perturbations in conjugated carbazole and naphthalimide-type frameworks are well known to alter charge-transfer character and excited-state polarization, owing to the sensitivity of the extended π-system to electronic effects.[34] Guided by these established structure–property relationships, electron-withdrawing groups (Br, NO_2, Cl, CN, CF_3, F, and OH) were introduced regioselectively at the 2,12-positions of the carbazole core (Fig. 1). This substitution pattern was chosen to maximize the perturbation of the molecular dipole vector while maintaining structural consistency across the series. The resulting JJ27 derivatives exhibit substantially enhanced dipole moments, ranging from 4.8 to 13.9 D. This increase is consistent with the strong inductive (−I) and, in some cases, resonance (−M) effects of halogenated and nitro substituents, which amplify molecular polarization.[35] The comparatively lower dipole moment observed for the OH-substituted derivative can be rationalized by its phenolic character, where resonance donation (+M) partially offsets its weak −I effect. Importantly, substitution at the 2,12-positions consistently produces larger dipole moments than analogous substitutions at the 5,9- or 3,11-positions found in the experimental systems, underscoring the critical role of regiochemical control in tuning molecular polarization. Collectively, this molecular set spans a broad, systematically tunable dipole range of approximately 2.7–13.9 D, providing an ideal platform for disentangling the relationship between molecular dipole strength and interfacial charge-transfer efficiency. Dipole moments values are tabulated in Table S1.

The electrostatic potential (ESP) maps shown in Fig. 2 provide direct insight into how peripheral functionalization

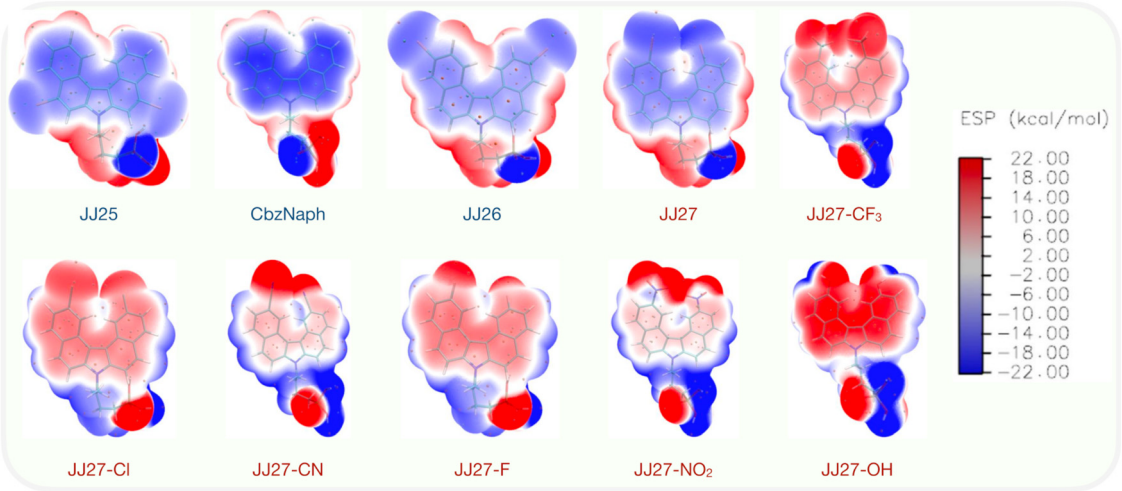

Fig. 2 Electrostatic potential (ESP) surfaces mapped onto the van der Waals molecular surface for CbzNaph, JJ25, JJ26, and the JJ27 derivative series (Br, CF_3, Cl, CN, F, NO_2, and OH substituents). The color scale ranges from −22 (blue, electron-rich regions) to +22 kcal mol^{-1} (red, electron-deficient regions). Substituent-dependent modulation of surface polarization is evident, demonstrating systematic tuning of the molecular dipole distribution through peripheral functionalization.

modulates the charge distribution of the carbazole scaffold. For the parent CbzNaph molecule, the π-conjugated aromatic framework displays a relatively uniform and moderately negative potential distributed across the extended carbon network. This balanced ESP pattern is consistent with delocalized electron density characteristic of conjugated aromatic systems and reflects the absence of strong local electron-withdrawing or -donating perturbations.

Upon substitution, however, pronounced changes in the surface potential become evident. Electron-withdrawing substituents such as NO_2, CN, CF_3, and halogens (F, Cl, Br) induce localized positive electrostatic potential at the substituted ring carbon, indicating depletion of electron density through dominant −I effects and, in certain cases, additional −M (resonance-withdrawing) contributions. In contrast, the OH-substituted derivative exhibits localized negative ESP regions in the vicinity of the oxygen atom, arising from lone-pair electron density and resonance donation (+M effect). This leads to partial stabilization of occupied orbitals and an enhancement of local nucleophilic character, distinguishing it from the strongly withdrawing derivatives. These substituent-dependent ESP variations qualitatively align with the trends observed in the electronic density of states (DOS). Electron-withdrawing groups generally lower the LUMO energy and alter the distribution of frontier orbitals, thereby modifying the effective electronic gap. Furthermore, the increasingly asymmetric ESP distributions in the more polar derivatives are consistent with their higher molecular dipole moments. Together, these observations confirm that targeted functionalization of the π-system provides systematic control over both molecular polarization and frontier electronic structure, laying the foundation for understanding their interfacial behavior.

The optimized interfacial geometries constructed for a representative SAM/ITO system are illustrated in Fig. 3a. The lower

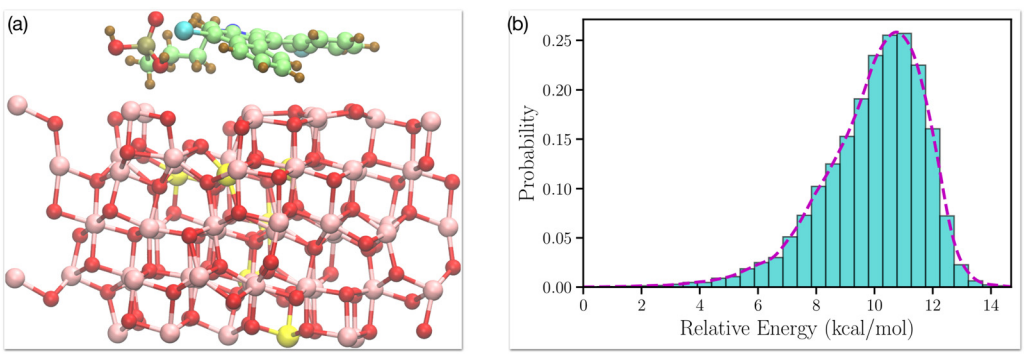

Fig. 3 (a) Optimized interfacial geometry of the JJ25 self-assembled monolayer on the ITO surface. The molecule adopts a predominantly face-on adsorption configuration, maximizing π–surface interaction and facilitating electronic coupling at the SAM–electrode interface. (b) Normalized probability density distribution of relative adsorption energies obtained from configurational sampling of SAM orientations on the ITO surface. The dashed line represents a Gaussian fit, highlighting the dominant low-energy adsorption regime and the statistical distribution of accessible interfacial conformations.

panel shows the atomistically resolved ITO slab, while the upper portion depicts the representative JJ25 molecule adsorbed on the surface. In all cases, the energetically preferred configuration corresponds to a predominantly face-on adsorption geometry, characterized by a finite molecular tilt, well-defined anchoring of the phosphonic acid group to the surface, and a specific vertical separation between the π-conjugated core and the electrode. These structural parameters directly influence interfacial dipole formation, electronic coupling, and the resulting work-function modulation.[9,36] Therefore, an accurate determination of adsorption geometry is essential for any mechanistic interpretation of interfacial energetics.

To rigorously assess the structural flexibility of the SAM/ITO interface, we performed an extensive conformational sampling using the XTB–GFN-FF framework. Although the initial adsorption geometry was optimized at the DFT level using CP2K, multiple low-energy orientations can exist in proximity to this minimum. The ITO slab atoms were fixed, and the equilibrium adsorption distance between the donor molecule and the surface was first identified. Around this optimized separation, a ±0.5 Å window was introduced, within which 10 000 conformers were generated by systematically varying molecular orientation and tilt. The relative energies of these configurations are summarized in Fig. 3b. The majority of sampled structures lie within ∼10 kcal mol^{-1} of the global minimum, and the total energy range explored spans 14.7 kcal mol^{-1}, indicating a moderately shallow interfacial potential energy surface. From this ensemble, the five lowest-energy conformers were extracted and compared with the CP2K-optimized structure using root-mean-square deviation (RMSD) analysis. The resulting RMSD values were minimal, confirming that the DFT-optimized geometry faithfully represents the thermodynamically most stable configuration. Notably, the CP2K-optimized structure was found to be even lower in energy than the minimum obtained from the force-field sampling, further validating its robustness.

Importantly, this computational finding provides a key, nuanced perspective on the hypothesis proposed in the experimental study, which invoked a predominantly vertical dipole orientation to explain enhanced PCE.[19] Our conformational analysis demonstrates that for an isolated adsorbate, such a perpendicular alignment does not correspond to the absolute thermodynamic minimum at the low-coverage SAM/ITO interface, where a face-on geometry is energetically favored. This distinction is critical, as the adsorption orientation governs the effective interfacial dipole component normal to the surface, electronic coupling with the electrode, and ultimately charge-transfer kinetics. The DFT-validated face-on configuration was therefore adopted as the primary baseline structural model for our electronic-structure and interfacial charge-transfer calculations. Nevertheless, because experimental SAMs under high-coverage conditions can undergo a morphological transition toward upright packing due to intermolecular forces, both this low-coverage face-on baseline and an alternative densely packed vertical configuration are systematically evaluated and contrasted in the subsequent sections to ensure a comprehensive assessment of the interface.

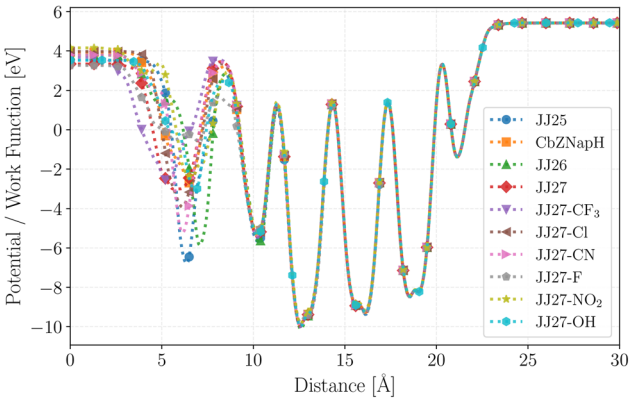

Fig. 4 Planar-averaged electrostatic potential profiles along the surface-normal direction for the bare ITO slab and SAM-functionalized interfaces. The vacuum level is identified from the plateau region at large distances, and the corresponding work function (Φ) is extracted from the difference between the vacuum potential and the Fermi level for each system.

The work function values were extracted from the planar-averaged electrostatic potential profiles (Fig. 4) according to $\Phi = E_{vac} - E_F$, where E_{vac} corresponds to the asymptotic vacuum level in the slab model and E_F denotes the Fermi energy. This methodology enables direct evaluation of vacuum-level alignment and quantification of interfacial dipoles at functionalized oxide surfaces.[37–39] In the ITO region, the oscillatory behavior of the electrostatic potential originates from the periodic stacking of cationic (In/Sn) and anionic (O) layers. The abrupt rise in potential at the surface marks the dipole barrier, from which the work function is determined.

As summarized in Table 1, all SAM-modified ITO interfaces exhibit work-function values within a narrow window of 5.407–5.424 eV, confirming that molecular adsorption induces only subtle but measurable modulation of the surface electrostatics. Although the absolute variation is slight, apparent substituent-dependent differences can be identified. The highest work function is obtained for JJ27–OH (5.424 eV), followed closely by CbzNaph (5.423 eV) and JJ27–F (5.421 eV), while JJ27 and the halogenated derivatives JJ27–Cl and JJ27–CN cluster around 5.420 eV. JJ27–NO_2 (5.416 eV) and JJ26 (5.413 eV) lie slightly lower, whereas JJ25 (5.411 eV) and particularly JJ27–CF_3 (5.407 eV) produce the smallest work-function values in the series. These results indicate that the work-function modulation does not follow a simple monotonic trend with nominal

Table 1 Calculated work function (Φ) values of ITO surfaces modified with different phosphonic acid–functionalized carbazole-based SAM molecules. The variations reflect substituent-dependent modulation of interfacial dipoles and vacuum-level shifts induced by molecular adsorption

SAM	Work function [eV]	SAM	Work function [eV]
JJ25	5.411	JJ27–Cl	5.420
CbzNaph	5.423	JJ27–CN	5.420
JJ26	5.413	JJ27–F	5.421
JJ27	5.420	JJ27–NO_2	5.416
JJ27–CF_3	5.407	JJ27–OH	5.424

electron-withdrawing strength. Instead, the observed variations reflect the combined influence of substituent-induced polarization, molecular orientation, and interfacial charge redistribution. While electron-withdrawing groups can enhance molecular dipoles and alter frontier orbital energies, their impact on the macroscopic work function depends on the orientation and net projection of the dipole normal to the surface, as well as on the extent of interfacial charge rearrangement.[40,41] For example, although CF_3 is strongly electron-withdrawing, JJ27–CF_3 yields the lowest Φ, indicating that its effective dipole contribution at the interface does not reinforce the surface dipole barrier. Conversely, JJ27–OH exhibits the highest work function, suggesting that its interfacial charge redistribution and dipole orientation produce a slightly stronger vacuum-level shift despite its moderate intrinsic electron-withdrawing character.

The parent systems JJ25, JJ26, JJ27, and CbzNaph fall within a narrow intermediate range, indicating moderate interfacial polarization. Overall, the limited spread of Φ values highlights the electrostatic rigidity of the ITO surface: the intrinsic oxide framework dominates the absolute work-function magnitude, while the SAM provides fine-tuning through chemically controlled dipole modulation. Consequently, substantial shifts in Φ require not only strong molecular dipoles but also favorable orientation and effective coupling to the surface electronic structure.

These observations are fully consistent with the charge-density-difference (CDD) analysis, which revealed predictable substituent-dependent polarization patterns at the interface. Notably, despite the limited absolute changes in Φ, the trends remain chemically systematic and reproducible. Furthermore, the total density of states (TDOS) profiles (Fig. S1) retain qualitatively similar spectral features across all systems, confirming that substitution modulates interfacial energetics without fundamentally altering the electronic structure of the conjugated carbazole backbone.

To gain deeper insight into the microscopic origin of the work-function modulation discussed above, the interfacial charge redistribution was analyzed through charge-density-difference calculations. The CDD is defined as $\Delta\rho = \rho(\text{SAM/ITO}) - \rho(\text{SAM}) - \rho(\text{ITO})$, where ρ(SAM/ITO) represents the total charge density of the combined interface, and ρ(SAM) and ρ(ITO) correspond to the isolated components in their interfacial geometries. The resulting isosurfaces (Fig. 5) therefore directly visualize electron accumulation and depletion induced by adsorption.

For the parent CbzNaph system, the CDD pattern reveals relatively localized charge redistribution confined to the phosphonic acid anchoring groups and adjacent aromatic regions, with minimal penetration into the ITO lattice. This behavior is characteristic of π-conjugated organic adsorbates interacting with metal-oxide surfaces predominantly through electrostatic interactions and dispersion forces, rather than through strong covalent hybridization.[42] The limited spatial extent of $\Delta\rho$ is consistent with the moderate dipole formation and correspondingly small work-function modification observed earlier. In contrast, the JJ26 and especially the JJ27 derivative series exhibit pronounced substituent-dependent variations in their CDD features. Strong electron-withdrawing groups such as NO_2, Cl, CN, and CF_3 generate larger cyan depletion regions along the SAM backbone, accompanied by distinct yellow accumulation lobes at the molecule–ITO contact region (Fig. 5 and Fig. S2). This pattern reflects enhanced dipole-induced charge rearrangement, whereby electron density is withdrawn from the conjugated framework and redistributed toward the interfacial region. The resulting polarization strengthens the local electrostatic perturbation at the surface and rationalizes the slightly elevated work functions for these systems. By comparison, F and OH substituents produce more diffuse and less intense CDD isosurfaces that extend toward the molecular periphery. This indicates weaker net charge displacement and reduced control over the surface electronic states of ITO. In the case of OH, partial resonance donation moderates the overall

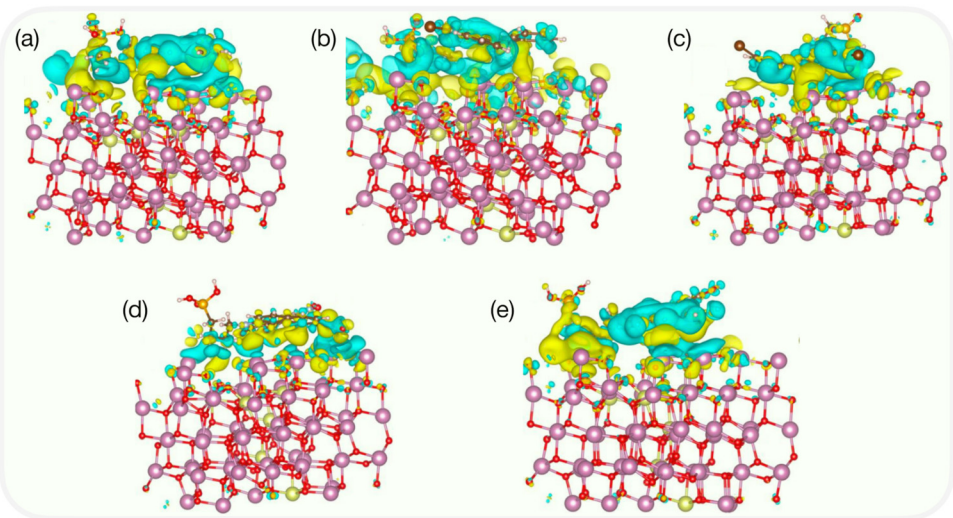

Fig. 5 Charge-density-difference (CDD) isosurfaces illustrating interfacial charge redistribution upon adsorption of SAM molecules on the ITO surface: (a) CbzNaph, (b) JJ25, (c) JJ26, (d) JJ27–NO_2, and (e) JJ27–OH. Yellow and cyan regions denote electron accumulation and depletion, respectively, highlighting substituent-dependent polarization and dipole formation at the molecule–oxide interface.

electron-withdrawing character, leading to a less pronounced interfacial dipole.

Overall, both the magnitude and spatial extent of $\Delta\rho$ across the JJ27 derivatives confirm that substituent-driven polarization is the principal factor governing the net dipole moment at the SAM/ITO interface. These microscopic charge rearrangements provide a direct electronic-structure explanation for the systematic trends in work-function shifts and, by extension, for variations in charge-injection barriers in oxide-based optoelectronic devices.[40,43] Thus, substituent chemistry emerges as a chemically tunable handle for modulating interfacial electronic structure and electron redistribution without fundamentally altering the backbone electronic framework.

The preceding analysis demonstrates that while dipole moments, electrostatic potential distributions, work-function shifts, and interfacial charge redistribution all exhibit systematic substituent dependence, none of these quantities alone establishes a direct correlation with the experimentally reported power conversion efficiencies. Notably, even the molecular dipole moments of the experimentally studied systems fail to reproduce the observed PCE trends, thereby challenging the previously proposed dipole-based design principle.[19] This discrepancy indicates that a more physically meaningful descriptor, that is, one directly connected to interfacial charge extraction kinetics, is required.

In this context, we evaluate the interfacial hole-transfer rate using the Marcus–Hush formalism,[44,45] which explicitly incorporates both the energetic driving force and the electronic coupling between donor and acceptor states. The required orbital energies, density-of-states information, and the electronic coupling elements were computed using the POD approach described in the Methods section (Fig. 6 and Fig. S3). The resulting energy offsets and charge-transfer rate constants are summarized in Table 2.

From Fig. 6, Fig. S3 and Table 2, the energy offset ΔE, defined as the difference between the SAM HOMO and the ITO Fermi level (E_F), serves as a measure of energetic alignment. A smaller magnitude of $|\Delta E|$ corresponds to a HOMO positioned closer to (E_F), thereby lowering the energetic barrier for hole transfer from the SAM to the electrode. Within classical Marcus theory, however, the charge-transfer rate constant depends not only on the driving force (which influences the activation barrier) but also on the square of the electronic coupling matrix element (J^2). Consequently, ΔE and the interfacial coupling strength jointly determine the overall transfer kinetics.

This interplay is clearly reflected in the computed rates. JJ25 exhibits one of the smallest $|\Delta E|$ values and correspondingly shows a relatively high hole-transfer rate (1.02×10^{13} s^{-1}), consistent with favorable energetic alignment. However,

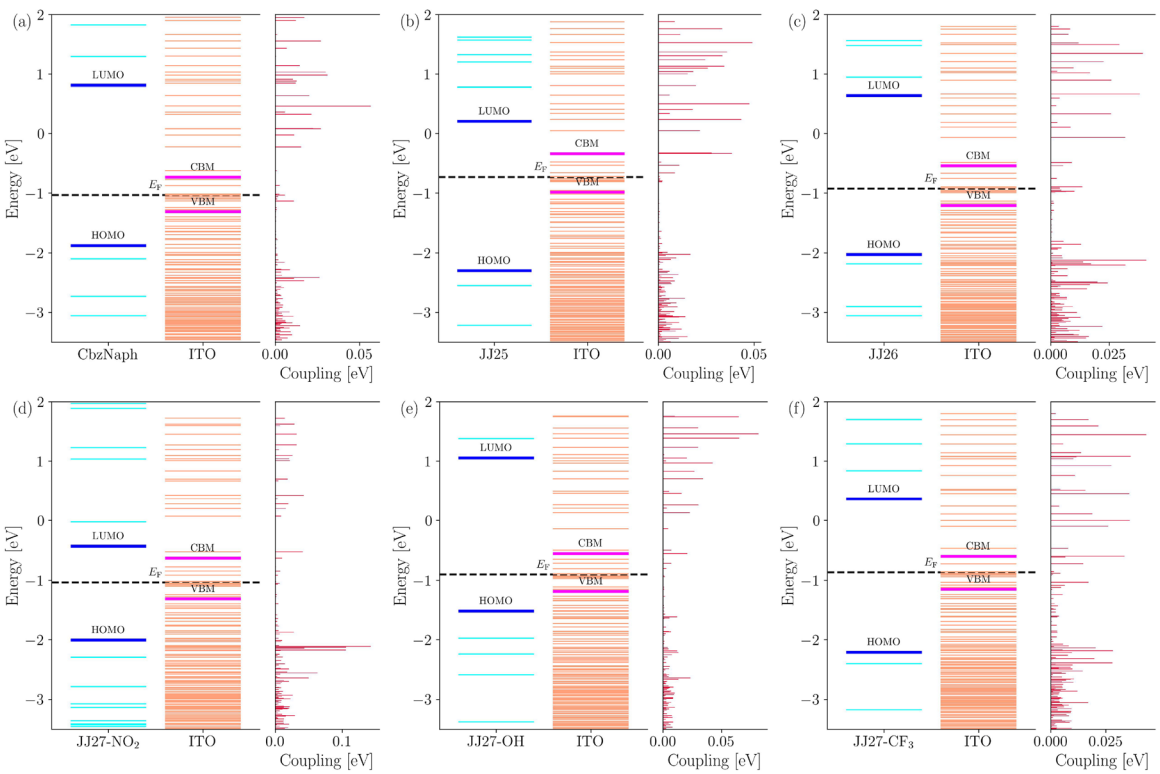

Fig. 6 Energy-level alignment and molecule–substrate electronic coupling at the SAM/ITO interfaces. Panels (a)–(f) correspond to CbzNaph, JJ25, JJ26, JJ27–NO_2, JJ27–OH, and JJ27–CF_3, respectively. The left column displays the molecular frontier orbitals with the HOMO and LUMO shown in blue. The central column presents the projected density of states (PDOS) of the ITO substrate, highlighting the valence band maximum (VBM) and conduction band minimum (CBM) in magenta. The right column illustrates the energy-resolved electronic coupling strength between the molecular orbitals and substrate states for each SAM/ITO interface.

Table 2 Calculated HOMO–Fermi level energy offset (ΔE) and corresponding interfacial hole-transfer rate constants for the investigated SAM/ITO interfaces, obtained within the Marcus–Hush formalism. The results highlight the combined influence of energetic alignment and electronic coupling on charge-transfer kinetics

Molecule	ΔE (eV)	Rate (s^{-1})	Molecule	ΔE (eV)	Rate (s^{-1})
JJ25	0.731	1.02×10^{13}	JJ27–Cl	0.993	4.07×10^{13}
CbzNaph	1.035	4.02×10^{12}	JJ27–CN	0.934	1.59×10^{13}
JJ26	0.927	3.82×10^{13}	JJ27–F	0.744	5.00×10^{13}
JJ27	0.802	1.76×10^{13}	JJ27–NO_2	1.038	7.19×10^{14}
JJ27–CF_3	0.872	4.23×10^{13}	JJ27–OH	0.905	4.02×10^{12}

JJ27–NO_2 presents a striking case: despite not possessing the smallest ΔE, it displays an exceptionally large transfer rate 7.19×10^{14} s^{-1}. Inspection of the coupling distributions in Fig. 6 reveals that JJ27–NO_2 exhibits significantly broader and more intense coupling features in the vicinity of E_F compared to the other derivatives. This indicates stronger interfacial hybridization and enhanced wavefunction overlap with ITO states, which substantially amplifies the J^2 contribution governing the transfer rate.[46]

Conversely, systems such as JJ27–OH and CbzNaph display comparatively lower transfer rates (on the order of 10^{12} s^{-1}), even though their ΔE values are not drastically different from those of other derivatives. Their coupling spectra are narrower and less intense near E_F, indicating fewer efficient charge-transfer channels. These results demonstrate that the energetic proximity of the HOMO to the Fermi level alone does not guarantee rapid hole extraction; sufficiently strong, spatially extended electronic coupling is equally critical.

The DOS analysis further shows that substituent-induced shifts in occupied molecular states systematically modulate the HOMO position relative to E_F, thereby tuning ΔE. Strong electron-withdrawing substituents (*e.g.*, NO_2, CF_3, CN) generally stabilize the HOMO, shifting it to lower energies, whereas weakly withdrawing or partially donating groups (*e.g.*, OH) tend to raise it. However, the coupling analysis reveals that substituent effects on interfacial hybridization can outweigh purely energetic considerations. Systems exhibiting stronger and more broadly distributed coupling elements near E_F possess enhanced tunneling probability and a higher density of accessible charge-transfer pathways, leading to accelerated interfacial kinetics.[9,47]

Taken together, the Marcus–Hush charge-transfer rate emerges as a physically meaningful descriptor that integrates both energy-level alignment and interfacial electronic coupling. Unlike dipole moment or work-function shifts considered in isolation, the computed rate constants directly quantify the efficiency of hole extraction at the SAM/ITO interface, thereby providing a mechanistically grounded parameter that can rationalize experimental PCE trends.

The preceding analysis established that strong acceptor substituents enhance interfacial hybridization, increase spectral overlap near the Fermi level, and promote stabilized charge redistribution at the SAM/ITO interface. These effects collectively strengthen the electronic coupling element and facilitate more efficient hole extraction. Having identified the Marcus–Hush charge-transfer rate as a physically meaningful descriptor, we now examine its relevance to experimentally measured device performance. Fig. 7 directly compares the calculated interfacial hole-transfer rate constants with the reported power conversion efficiencies for two device architectures, PM6/BTP-eC9:dT9TBO and D18/L8-BO:Y6-OBO (see Table S2 for full device metrics including J_{SC}). The cyan curve represents the logarithm of the computed rate constants, while the blue and red dotted curves denote the corresponding experimental PCE values. Notably, both device systems exhibit a similar monotonic increase in PCE from CbzNaph to JJ26. In particular, JJ26 delivers the highest efficiencies in both blends (19.27% for PM6/BTP-eC9:dT9TBO and 19.35% for D18/L8-BO:Y6-OBO), consistent with its comparatively large calculated transfer rate. Conversely, CbzNaph displays both the smallest rate constant and the lowest experimental PCE among the examined systems. This qualitative agreement between POD-derived charge-transfer rates and experimental efficiencies indicates a positive correlation between interfacial charge-extraction kinetics and overall photovoltaic performance. Importantly, this correlation is not captured by any single ground-state electronic property considered in isolation; neither dipole moment nor work-function shift alone reproduces the experimental ranking. Instead, the rate constant intrinsically integrates the relevant interfacial descriptors: (i) orbital energetics through ΔE, (ii) molecular polarization and dipole-induced electrostatics, and (iii) electronic coupling strength arising from interfacial hybridization. The synergy among these factors governs the activation barrier and tunneling probability, thereby directly impacting charge separation and extraction efficiency.

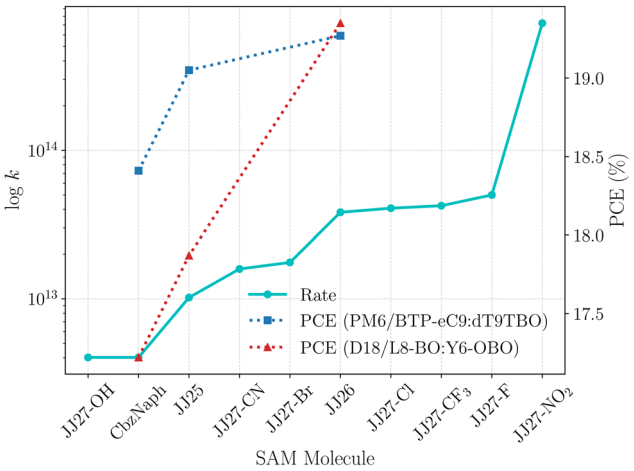

Fig. 7 Correlation between calculated interfacial hole-transfer rate constants and experimentally reported power conversion efficiencies (PCEs) for different SAM-modified devices. The cyan solid line (left axis) represents the logarithm of the computed rate constants ($\log k$), while the blue and red dotted lines (right axis) correspond to the experimental PCE values for PM6/BTP-eC9:dT9TBO and D18/L8-BO:Y6-OBO devices, respectively. The plot highlights the relationship between interfacial charge-transfer kinetics and photovoltaic performance.

Strong electron-withdrawing substituents, such as NO_2, generate large molecular dipoles (up to 13.96 D for JJ27–NO_2),

stabilize frontier orbitals, and produce pronounced coupling features near E_F. This combination creates a steep energetic gradient and ultra-fast hole-transfer kinetics. In contrast, weakly withdrawing substituents yield shallower energetic gradients, less intense coupling distributions, and slower transfer rates. The overall trend demonstrates that substituent chemistry modulates not only molecular polarization but also the interfacial electronic structure in a concerted manner. By integrating electrostatics, energy-level alignment, and coupling into a single kinetic descriptor, the present analysis establishes interfacial charge-transfer rate as a robust structure–property–performance metric. Targeted chemical functionalization of the JJ27 framework, therefore, emerges as a rational strategy to tune interfacial electrostatics, work-function modulation, and charge-transfer kinetics in a unified manner, ultimately enabling predictive control over device performance.

Subsequently, to evaluate the structural robustness of the identified kinetic trends and extend our microscopic model toward highly packed experimental conditions, we expanded our computational framework beyond the isolated, low-coverage adsorption regime. On a clean metal-oxide surface, a solitary organic adsorbate naturally maximizes its spatial contact area, resulting in a thermodynamically favored ''face-on'' (flat-lying) geometry driven by direct π-orbital hybridization with the substrate surface. However, under experimental high-coverage conditions, dense surface anchoring and intermolecular van der Waals packing forces constrain the molecular backbones into a vertically aligned, ''standing-up'' orientation.

To explicitly isolate the electronic consequences of this morphological transition, we constructed and optimized a dense, vertically aligned two-molecule periodic configuration for the experimental series (CbzNaph, JJ25, and JJ26). This model introduces realistic steric constraints and forces the hole-extraction pathway to proceed *via* a tunneling mechanism, primarily mediated by the deprotonated phosphonic acid anchoring backbone, contrasting with the direct core-to-substrate coupling that dominates the face-on configuration. The non-adiabatic interfacial electron-transfer rates (k_{ET}) computed *via* the Marcus–Hush formalism for both structural configurations are summarized in Table 3, along with their corresponding experimental power conversion efficiencies.

An analysis of the kinetic data reveals two profound physical insights. First, transitioning from a face-on to a vertical orientation induces a noticeable modulation in the absolute magnitudes of the electronic coupling matrix elements [$J(E)$]. For CbzNaph and JJ25, the absolute extraction rates decrease slightly in the vertical phase, reflecting the expected operational tunneling barrier imposed by the aliphatic/phosphonic acid anchoring segment when direct core-π hybridization is severed. Second, and most critically, the qualitative and quantitative ordering of the charge-extraction efficiency remains completely invariant between both structural regimes, strictly matching the experimental device trend:

$$\text{CbzNaph} < \text{JJ25} < \text{JJ26}$$

Rather than disrupting the observed trends, forcing an upright orientation demonstrates that the electronic influence of different halogen substituents systematically propagates throughout the molecular framework, altering wave-function amplitudes even at the σ-bonded phosphonic acid anchoring site. The invariance of this relative performance ordering across completely distinct spatial configurations confirms that our identified descriptors capture intrinsic electronic features of the hybrid interface rather than geometric artifacts of an isolated model.

While the tuning of interfacial dipoles *via* peripheral substitution and the broad application of Marcus–Hush kinetics are well-established concepts in surface science, their integration here serves to challenge a pervasive design paradigm in the organic electronics and photovoltaic communities. In conventional device optimization, macroscopically derived properties such as the net vertical dipole moment of an isolated molecule or the resulting shift in the substrate work function, are heavily relied upon as monotonic predictors of charge-extraction efficiency. Our comparative analysis of the ''face-on'' and ''vertical'' configurations systematically demonstrates the limitations of these macroscopic assumptions, showing they are fundamentally insufficient for predicting device performance. Whether charge extraction proceeds *via* direct core contact or *via* anchor-mediated tunneling, a simple dipole-moment descriptor fails to predict the experimental performance sequence. Instead, the ultimate arbiter of charge extraction across both structural regimes is the subtle, substituent-dependent modulation of the quantum-mechanical coupling matrix elements, $J(E)$.

To contextualize the alignment of our first-principles kinetic parameters with macroscopic device performance, it is necessary to examine the multiscale physics governing the operation of solar cells. Experimentally measured macroscopic parameters, such as the full-device power conversion efficiency (PCE), represent a complex convolution of multiple sequential, interdependent photophysical processes. These include photon absorption, bulk exciton diffusion, charge separation at the heterojunction, non-geminate recombination, and carrier drift-diffusion through macroscopic transport layers. Our quantum-mechanical model deliberately isolates and probes exactly one fundamental bottleneck in this multi-step cascade: the microscopic hole-extraction kinetics (k_{ET}) at the immediate functionalized SAM/ITO boundary. Because this first-principles framework does not explicitly simulate macroscopic carrier drift, thin-film morphology defects, or bulk recombination

Table 3 Influence of molecular configuration on the calculated interfacial electron-transfer rates (k_{ET}) and their correlation with experimental device performance

		One molecule (Face-on)		Two molecules (Vertical)	
SAM	PCE (%)	k_{ET} (s^{-1})	$\log_{10}(k_{ET})$	k_{ET} (s^{-1})	$\log_{10}(k_{ET})$
CbzNaph	18.41	4.02×10^{12}	12.60	5.778×10^{11}	11.76
JJ25	19.05	1.02×10^{13}	13.01	6.210×10^{12}	12.79
JJ26	19.27	3.82×10^{13}	13.58	5.856×10^{13}	13.77

resistances, the calculated transfer rate functions as an intrinsic, idealized material interface descriptor. Remarkably, despite these macroscopic omissions, this isolated electronic descriptor yields a strong, monotonic qualitative correlation that perfectly mirrors the experimentally reported device sequence. This robust correlation underscores the predictive utility of microscopic charge-transfer kinetics as a reliable, high-throughput screening metric for the rational design and electronic optimization of interfacial interlayers.

4 Conclusion

A comprehensive structure–property analysis was conducted to elucidate how molecular functionalization governs interfacial electronic structure and, ultimately, charge-extraction efficiency at the SAM/ITO interface. While ground-state descriptors, such as dipole moments and electrostatic potential distributions, provide valuable insight into molecular polarization, our results demonstrate that these parameters alone are insufficient to rationalize experimentally observed device trends. Instead, interfacial performance emerges from the concerted interplay between electrostatics, energy-level alignment, and electronic coupling. Molecules exhibiting strong, spatially well-defined charge asymmetry exhibit enhanced interfacial polarization, as reflected in their ESP profiles and dipole moments. Among the investigated derivatives, JJ27–NO_2 displays the most pronounced polarization and the largest dipole moment, leading to a substantial interfacial electrostatic gradient. However, the decisive factor is not polarization in isolation, but how it translates into favorable orbital alignment and interfacial hybridization. Work function and density-of-states analyses confirm that substituent-induced electrostatic modulation systematically tunes the HOMO position relative to the ITO Fermi level, thereby influencing the energetic driving force for hole extraction.

Crucially, quantitative evaluation within the Marcus–Hush framework reveals that the interfacial charge-transfer rate, rather than dipole moment or work function shift alone, serves as the most physically meaningful descriptor. The rate constant inherently integrates the energetic offset and the electronic coupling element (J), capturing both activation barrier effects and wavefunction overlap. The validity of this non-adiabatic tunneling framework across these hybrid boundaries is directly justified by our electronic structure data. As evidenced by the projected density of states (PDOS) in Fig. S1 and the explicit density of states mapping from our POD analysis, the localized molecular orbitals of the ligand remain energetically distinct from the valence and conduction states of the ITO substrate. This clear separation confirms that the interface operates within a weak-coupling, non-adiabatic regime rather than a strongly hybridized adiabatic state, justifying our use of the energetic offset as the driving force under short-circuit conditions ($\eta = 0$). Within this unified kinetic framework, systems combining favorable energetic alignment with strong interfacial coupling exhibit markedly enhanced hole-transfer kinetics. In this regard, JJ27–NO_2 consistently demonstrates the largest calculated rate constant, indicating superior intrinsic charge-extraction capability, whereas weakly polarized systems with limited coupling display slower kinetics.

Notably, the computed rate constants show qualitative agreement with experimentally reported power conversion efficiencies, establishing a direct structure–kinetics–performance relationship. Importantly, extended evaluations demonstrating that this relative performance sequence (CbzNaph < JJ25 < JJ26) remains completely invariant across both the thermodynamic face-on arrangement and a vertically aligned packed monolayer configuration explicitly confirm that our kinetic conclusions are structurally robust and independent of a specific spatial motif. This correlation confirms that efficient device operation is governed by synergistic optimization of molecular polarization, orbital energetics, and interfacial electronic coupling, and not by any single parameter in isolation. Overall, the present study constructs a unified multilevel framework linking chemical functionalization to interfacial electrostatics, electronic structure, and charge-transfer dynamics, providing an operationally relevant guideline for the rational design of practical optoelectronic interlayers.

Author contributions

AM conceived the problem. HS conducted all the simulations. HS and AM analyzed the results and prepared the draft.

Conflicts of interest

There are no conflicts to declare.

Data availability

All data supporting the findings of this study are available within the article and its supplementary information (SI). Supplementary information: dipole moments, experimentally measured metrics, density-of-states, charge-density difference, and energy-level-coupling plots. See DOI: https://doi.org/10.1039/d6tc02069k.

Additional datasets are available from the corresponding authors upon reasonable request.

Acknowledgements

The authors gratefully acknowledge the Indian Institute of Technology Gandhinagar, India, for providing research facilities and financial support. We thank PARAM Ananta for computational resources.

References

1 S. R. Forrest, The path to ubiquitous and low-cost organic electronic appliances on plastic, *Nature*, 2004, **428**, 911–918.
2 A. Facchetti, Polymer donor–polymer acceptor (all-polymer) solar cells, *Mater. Today*, 2013, **16**, 123–132.

3 C. J. Brabec, S. Gowrisanker, J. J. Halls, D. Laird, S. Jia and S. P. Williams, Polymer–fullerene bulk-heterojunction solar cells, *Adv. Mater.*, 2010, **22**, 3839–3856.

4 M. Pope and C. E. Swenberg, *Electronic Processes in Organic Crystals and Polymers*, Oxford University Press, 1999.

5 V. I. Arkhipov, U. Wolf and H. Bässler, Current injection from a metal to a disordered hopping system. II. Comparison between analytic theory and simulation, *Phys. Rev. B:Condens. Matter Mater. Phys.*, 1999, **59**, 7514.

6 M. Azzouzi, N. P. Gallop, F. Eisner, J. Yan, X. Zheng, H. Cha, Q. He, Z. Fei, M. Heeney, A. A. Bakulin and J. Nelson, Reconciling models of interfacial state kinetics and device performance in organic solar cells: impact of the energy offsets on the power conversion efficiency, *Energy Environ. Sci.*, 2019, **12**, 1237–1247.

7 Y. Tamai, R. Shirouchi, T. Saito, K. Kohzuki and S. Natsuda, Role of the energy offset in the charge photogeneration and voltage loss of nonfullerene acceptor-based organic solar cells, *Energy Environ. Sci.*, 2019, **12**, 3287–3296.

8 A. A. Bakulin, A. Rao, V. G. Pavelyev, P. H. van Loosdrecht, M. S. Pshenichnikov, D. Niedzialek and R. H. Friend, The role of driving energy and delocalized states for charge separation in organic semiconductors, *Science*, 2012, **335**, 1340–1344.

9 H. Ishii, K. Sugiyama, E. Ito and K. Seki, Energy level alignment and interfacial electronic structures at organic/metal and organic/organic interfaces, *Adv. Mater.*, 1999, **11**, 605–625.

10 N. Koch, Energy levels at interfaces between metals and conjugated organic molecules, *J. Phys.: Condens. Matter*, 2008, **20**, 184008.

11 J. D. Myers and J. Xue, Organic semiconductors and their applications in photovoltaic devices, *Polym. Rev.*, 2012, **52**, 1–37.

12 X. E. Li, Q. Zhang, J. Yu, Y. Xu, R. Zhang, C. Wang and M. Fahlman, Mapping the energy level alignment at donor/acceptor interfaces in non-fullerene organic solar cells, *Nat. Commun.*, 2022, **13**, 2046.

13 R. J. Davis, M. T. Lloyd, S. R. Ferreira, M. J. Bruzek, S. E. Watkins, L. Lindell and J. W. Hsu, Determination of energy level alignment at interfaces of hybrid and organic solar cells under ambient environment, *J. Mater. Chem.*, 2011, **21**, 1721–1729.

14 K. Patrikar and A. Mondal, Polarity and orbital driven reduction in contact resistance in organic devices with functionalized electrodes, *J. Chem. Phys.*, 2023, **159**, 121102.

15 J. Zou, C. Z. Li, C. Y. Chang, H. L. Yip and A. K. Y. Jen, Interfacial engineering of ultrathin metal film transparent electrode for flexible organic photovoltaic cells, *Adv. Mater.*, 2014, **26**, 3618–3623.

16 E. Ratcliff; B. Zacher; X. Steirer; J. Gantz; G. MacDonald; M. Macech and N. R. Armstrong The interface science of interlayer materials and contacts in organic solar cells. roc. IEEE Photovolt. Spec. Conf. 2011; pp 003472–003476.

17 N. Nurfitria, Y.-T. Tao and D.-C. Huang, Work Function Modulation with Self-assembled Monolayers: Effect of Dipole Moment on Packing Density, 1st International Seminar on Science and Technology 2015, Surabaya, Indonesia, August 2015, Sepuluh Nopember Institute of Technology.

18 H. Liu, Y. Xin, Z. Suo, L. Yang, Y. Zou, X. Cao and Y. Chen, Dipole moments regulation of biphosphonic acid molecules for self-assembled monolayers boosts the efficiency of organic solar cells exceeding 19.7%, *J. Am. Chem. Soc.*, 2024, **146**, 14287–14296.

19 W. Jiang, Y. Li, H. Gao, L. Kong, C. T. Wong, X. Yang and A. K. Y. Jen, Regiospecific halogenation modulates molecular dipoles in self-assembled monolayers for high-performance organic solar cells, *Angew. Chem., Int. Ed.*, 2025, e202502215.

20 C. Yan, S. Barlow, Z. Wang, H. Yan, A. K. Y. Jen, S. R. Marder and X. Zhan, Non-fullerene acceptors for organic solar cells, *Nat. Rev. Mater.*, 2018, **3**, 1–19.

21 J. Yi, G. Zhang, H. Yu and H. Yan, Advantages, challenges and molecular design of different material types used in organic solar cells, *Nat. Rev. Mater.*, 2024, **9**, 46–62.

22 B. Fan, H. Gao, L. Yu, R. Li, L. Wang, W. Zhong and A. K. Y. Jen, Local structure-induced selective interactions enables high-performance and burn-in-free organic photovoltaics, *Angew. Chem., Int. Ed.*, 2025, **64**, e202418439.

23 K. Patrikar and A. Mondal, Understanding the Microscopic Origin of the Contact Resistance at the Polymer–Electrode Interface, *ACS Appl. Mater. Interfaces*, 2025, **17**, 32306–32315.

24 Z. Futera and J. Blumberger, Electronic couplings for charge transfer across molecule/metal and molecule/semiconductor interfaces: Performance of the projector operator-based diabatization approach, *J. Phys. Chem. C*, 2017, **121**, 19677–19689.

25 W. Kohn and L. J. Sham, Self-consistent equations including exchange and correlation effects, *Phys. Rev.*, 1965, **140**, A1133.

26 M. Nurhuda, C. C. Perry and M. A. Addicoat, Performance of GFN1-xTB for periodic optimization of metal organic frameworks, *Phys. Chem. Chem. Phys.*, 2022, **24**, 10906–10914.

27 J. Hutter, M. Iannuzzi, F. Schiffmann and J. VandeVondele, CP2K: atomistic simulations of condensed matter systems, *WIREs Comput. Mol. Sci.*, 2014, **4**, 15–25.

28 J. P. Perdew, K. Burke and M. Ernzerhof, Generalized gradient approximation made simple, *Phys. Rev. Lett.*, 1996, **77**, 3865.

29 C. Hartwigsen, S. Goedecker and J. Hutter, Relativistic separable dual-space Gaussian pseudopotentials from H to Rn, *Phys. Rev. B:Condens. Matter Mater. Phys.*, 1998, **58**, 3641.

30 S. Goedecker, M. Teter and J. Hutter, Separable dual-space Gaussian pseudopotentials, *Phys. Rev. B:Condens. Matter Mater. Phys.*, 1996, **54**, 1703–1710.

31 Y. A. Berlin, G. R. Hutchison, P. Rempala, M. A. Ratner and J. Michl, Charge hopping in molecular wires as a sequence of electron transfer reactions, *J. Phys. Chem. A*, 2003, **107**, 3970–3980.

32 M. J. Frisch; G. W. Trucks; H. B. Schlegel; G. E. Scuseria; M. A. Robb; J. R. Cheeseman and H. Nakatsuji, *Gaussian 09*, Gaussian, Inc., 2009.

33 G. Kresse and J. Furthmüller, Efficient iterative schemes for ab initio total-energy calculations using a plane-wave basis

set, *Phys. Rev. B:Condens. Matter Mater. Phys.*, 1996, **54**, 11169.
34 N. Chen and B. Yan, Recent theoretical and experimental progress in circularly polarized luminescence of small organic molecules, *Molecules*, 2018, **23**, 3376.
35 H. H. Jaffe, A reexamination of the Hammett equation, *Chem. Rev.*, 1953, **53**, 191–261.
36 J. Bertrandie, J. Han, C. S. De Castro, E. Yengel, J. Gorenflot, T. Anthopoulos and D. Baran, The energy level conundrum of organic semiconductors in solar cells, *Adv. Mater.*, 2022, **34**, 2202575.
37 H. Yoshida, Electron transport in bathocuproine interlayer in organic semiconductor devices, *J. Phys. Chem. C*, 2015, **119**, 24459–24464.
38 G. Sun, J. Kürti, P. Rajczy, M. Kertesz, J. Hafner and G. Kresse, Performance of the Vienna ab initio simulation package (VASP) in chemical applications, *J. Mol. Struct. THEOCHEM*, 2003, **624**, 37–45.
39 J. Neugebauer and M. Scheffler, Adsorbate-substrate and adsorbate-adsorbate interactions of Na and K adlayers on Al (111), *Phys. Rev. B:Condens. Matter Mater. Phys.*, 1992, **46**, 16067–16080.
40 G. Heimel, S. Duhm, I. Salzmann, A. Gerlach, A. Strozecka, J. Niederhausen and N. Koch, Charged and metallic molecular monolayers through surface-induced aromatic stabilization, *Nat. Chem.*, 2013, **5**, 187–194.
41 J. Meyer, S. Hamwi, M. Kröger, W. Kowalsky, T. Riedl and A. Kahn, Transition metal oxides for organic electronics: energetics, device physics and applications, *Adv. Mater.*, 2012, **24**, 5408–5427.
42 H. Wahnou, R. El Kebbaj, B. Liagre, V. Sol, Y. Limami and R. E. Duval, Curcumin-based nanoparticles: advancements and challenges in tumor therapy, *Pharmaceutics*, 2025, **17**, 114.
43 R. Otero, A. V. De Parga and J. M. Gallego, Electronic, structural and chemical effects of charge-transfer at organic/inorganic interfaces, *Surf. Sci. Rep.*, 2017, **72**, 105–145.
44 R. A. Marcus, On the Theory of Oxidation-Reduction Reactions Involving Electron Transfer, *J. Chem. Phys.*, 1956, **24**, 966–978.
45 R. A. Marcus and N. Sutin, Electron Transfers in Chemistry and Biology, *Biochim. Biophys. Acta*, 1985, **811**, 265–322.
46 A. Nitzan, Electron Transmission Through Molecules and Molecular Interfaces, *Annu. Rev. Phys. Chem.*, 2001, **52**, 681–750.
47 A. Kahn, N. Koch and W. Gao, Electronic Structure and Electrical Properties of Interfaces Between Metals and π-Conjugated Molecular Films, *J. Polym. Sci., Part B: Polym. Phys.*, 2003, **41**, 2529–2548.